Test and Analysis of a New Ductile Shear Connection Design for RC Shear Walls

Sørensen, Jesper Harrild; Hoang, Linh Cao; Olesen, John Forbes; Fischer, Gregor

Published in:
Structural Concrete

Link to article, DOI:
10.1002/suco.201600056

Publication date:
2017

Document Version
Early version, also known as pre-print

Test and Analysis of a New Ductile Shear Connection Design

Jesper H. Sørensen, Linh C. Hoang, John F. Olesen, Gregor Fischer

Technical University of Denmark, Department of Civil Engineering, Brovej, Bygning 118, 2800 Kgs. Lyngby, Denmark

Abstract

This paper presents a new and construction-friendly shear connection for assembly of precast shear wall elements. In the proposed design, the precast elements have indented interfaces and are connected by a narrow zone grouted with mortar and reinforced with overlapping U-bar loops. Contrary to the classical shear connections, the planes of the U-bar loops are here parallel to the plane of the wall elements. This feature enables a construction-friendly installation of the elements without the risk of rebars clashing. The core of mortar inside each U-bar loop is reinforced with a transverse double T-headed bar to ensure transfer of tension between the overlapping U-bars. Push-off tests show that a significantly ductile load-displacement response can be obtained by the new solution as compared to the performance of the conventional keyed shear connection design. The influence of the interface indentation geometry was investigated experimentally and the failure modes in the push-off tests were identified by use of digital image correlation (DIC). For strength prediction, rigid plastic upper bound models have been developed with inspiration from the observed failure mechanisms. Satisfactory agreement between tests and calculations has been obtained.

Keywords: Keyed Shear Connections, Ductility, Robustness, Concrete Plasticity, Digital Image Correlation

1. Introduction

Structural solutions based on precast concrete elements are often more economically feasible than in-situ cast solutions. The reason is, that the precast technology enables a reduction of the construction time as well as the labor cost. When using precast solutions, the on-site work primarily comprises of assembling and connecting the precast elements into an integrated structural system. Hence, connection designs that are construction-friendly play an important role for the overall cost reduction. It is, however, a challenge to design connections that are construction-friendly and at the same time have structural performance (in terms of strength and ductility) which can be compared to that of in-situ cast solutions. In cases with unusual structural geometry, it may be necessary to supplement the advantages of precast construction with in-situ cast solutions in selected zones. An example of how current precast solutions have been pushed to the limit can be studied in Refs. [1, 2], which report on the design and construction of a landmark building in Copenhagen, Denmark. The leaning characteristic of the building imposed serious challenges to the design of the shear connections between the precast panels for insurance of overall structural stability.

Currently, the structural continuity between precast shear panels is established by use of narrow keyed connections containing overlapping U-bars and grouted with mortar (see Figure 1). However, with this classical solution, which has been used since the 1960's, it is difficult to obtain full structural continuity because the strength and ductility of the connection will normally be less than that of the precast elements [3, 4]. In addition, the construction sequence is influenced by the design. To avoid rebar-clashing when assembling the precast panels, see Figure 1(b), the U-bars protruding from the precast panels have to be bent up (prior to installation of panel)

and subsequently straightened again, once the panel has been placed in position. This procedure imposes a limit on the cross sectional diameter of the U-bars and hence limits the strength of the connection (normally bars with diameter 6-8 mm are used). The classical shear connection is therefore not feasible for use in shear walls of e.g. tall buildings, where considerable horizontal loads have to be carried.

This paper presents a new solution for the connection of precast shear wall elements. The aim of the new design is to ease the construction challenges and at the same time improve the structural performance, as compared to the classical solution. Figure 2 schematically illustrates the new connection design which differs from the classical solution in the way the U-bar loops are oriented and in the way structural continuity in the U-bar overlaps is ensured. The joint interfaces are keyed like in the classical solution. As illustrated in Figure 2, the loop orientation in the new solution allows for a construction-friendly installation (vertical lowering) of the precast panels without clashing of rebars and thus without the need to pre-bend and post-straighten the U-bars. For this reason, U-bars with larger diameters than 8 mm can be used. In addition to a single longitudinal lock bar, the new design also includes the use of transverse lock bars (in the following called lacer bars) in the form of a double T-headed rebar placed inside the U-bar loops. The idea here is to utilize the double headed rebar together with the core of mortar inside the loop as a transverse dowel that enables transfer of tension between the overlapping U-bars. Tension in the U-bars across the connection is required to ensure equilibrium when diagonal compression struts develop between the keyed joint interfaces as a result of shear loading. The double T-headed rebar is chosen because the heads provide increased anchorage of the short lacer reinforcement, which otherwise cannot be ensured using regular straight reinforcement.

To investigate the structural performance of the new connection design, an exper-

imental program has been conducted. The investigation showed that the load-displacement response of the new design is significantly more ductile than that of the classical solution. Furthermore, the tests indicated that it is possible to obtain larger load carrying capacities with the new design. In addition to the experimental work, this paper also presents upper bound rigid-plastic models for prediction of the critical failure mode as well as the load carrying capacity of the new connection design. The models furnish a simple tool to optimize the geometry of the keyed joint interfaces in order to enhance the ductile behavior of the connection.

2. Previous Investigations on Shear Connections

With the introduction of precast element construction, the design and performance of on-site cast connections became a matter of special interest. Since the 1960's, the classical keyed shear connection has been experimentally investigated, where the main interests have been on the behavior of the connection during loading, the ultimate load carrying capacity, and the design aspects of the joint configuration. Hansen et al. [4] summarized the early work on this topic in a report, which constitutes the work of the CIB commission W23A. The experimental programs that served as basis for the commissions report include the work of Halasz and Tantow, Cholewicki, Pommeret, Fauchart and Cortini [5–8] who used similar test setups as the one used in the present study. Shear tests with other test setups to investigate factors that influence the load carrying capacity have also been published [9–14]. In all investigations, regardless of testing method, it was recognized that the ultimate capacity was influenced by a number of factors, including the number of shear keys, the cross sectional area of the keys, the strength of the grout mortar, the degree of transverse reinforcement, and the magnitude of external transverse confinement stresses.

Based on the experimental findings, a number of semi-empirical formulas were suggested for prediction of the ultimate load carrying capacity. Current design provisions for joints between concrete cast at different times are based on the shear friction hypothesis, see e.g. the *fib* guide to good practice [3] and the European code of practice [15]. However, other approaches can also be used. Kaneko et al. [16, 17] proposed a fracture mechanics approach to predict the crack formation in indented shear joints. They identified two main fracture mechanisms for shearing of keys, based on an experimental program that included plain and fiber reinforced concrete joints. The test results were supplemented with nonlinear FEM calculations. Later, Kaneko and Mihashi [18] extended the investigation by presenting an analytical model for determination of the transition between the two mechanisms. However, variations in key dimensions such as length and depth were not included in the experimental investigation.

Theoretical works based on the theory of rigid-plasticity have also been proposed. Jensen [19] was the first to establish an upper bound solution for the load carrying capacity of keyed shear joints by assuming complete shearing of the key area. These findings have later on been the basis for several simplified formulas, which incorporate empirical factors to fit theory with test results. This includes the formulas by Chakrabarti et al. [20] and Abdul-Wahab and Sarsam [21]. Later Christoffersen [22] expanded the application of plasticity theory to include both upper and lower bound solutions for the shear capacity of keyed joints. Recently, Jørgensen and Hoang [23] developed an upper bound model for the failure of keyed shear joints reinforced with high strength wire rope loops by accounting for diagonal cracks between the shear keys. Jensen, Christoffersen as well as Jørgensen and Hoang only considered a global failure mechanism with complete shearing of the keyed area. A local failure mode that involves key corner crushing has been observed by several authors. However, the

problem has not been treated in depth, nor has an analytical solution been proposed.

3. Experimental Program

The experimental program contained a total of 25 push-off tests. The program included a preliminary investigation of 7 specimens where the performance of the classical design, as a reference, was compared to the new design with identical geometrical joint properties. The remaining 18 specimens, series I-IX, were subdivided into two investigations related to the geometry of the key indentation, see Figure 3. The tests were carried out in quasi-static deformation control.

3.1. Specimens and Geometry

The general geometry of the push-off test specimens can be seen in Figure 3 and details of geometrical and material properties are given in Table 1. Series R refers to *reference* specimens designed with a classical reinforcement layout as illustrated in Figure 1(a) (however, in the reference specimens, the loops were placed outside the keyed area). Series P refers to *pilot* specimens designed with '2-on-1' vertical loop connections. This means a design similar to the principles shown in Figure 2(a), however, in the pilot specimens, there was (for each looped connection) only one centrally placed U-bar which protruded from the precast element to the right. The cross sectional area of this single U-bar is referred to as A_s in Table 1. The reinforcement area, A_s, as well as the geometry of the shear keys were identical for all specimens in series R and P. The joints in series P were not provided with longitudinal locking bars. For specimens type I to IX, '2-on-2' vertical loop connections were used, see Figure 2(a). For these specimens the area A_s listed in Table 1 should be understood as the cross sectional area of two U-bars. In order to eliminate the edge effect, anchorage plates were mounted at each end of the longitudinal locking bar in

series I to IX. In 8 specimens (series I-IV), the length of the keys, L_k, was varied while the key height, h_k, was kept constant to half of the panel thickness, t. In the remaining 10 specimens (series V-IX), the depth of the key indentation, d_k, was varied while the key length and the key height were kept constant, $L_k = 140\ mm$ and $h_k = 200\ mm$. Table 2 contains parameters and material properties for Series I-IX. The diameter of the lacer bar was carefully designed so that the tensile capacity of the overlapping loops would be governed by yielding of the U-bars and not crushing of the mortar. For this purpose, the calculation model for tensile capacity of U-bar loop connections developed by Jørgensen and Hoang [24] was used. The double T-headed lacer bar in each loop was positioned as shown in figure 2(a) to make it function as tension reinforcement in the small transverse circular mortar dowel, that ensures transfer of tension between the overlapping U-bars. Each design was tested with 2 replicates and the material properties were found as average values obtained from tensile tests of the steel reinforcement and compression tests of ϕ100x200 mm cylinders of the mortar used for casting the joints.

3.2. Digital Image Correlation

In the present investigation, digital image correlation (DIC) was used to study the relative displacements on the surface of the shear connection, including development of cracks in the joint mortar. The analysis was performed by use of the Aramis software [25]. An example of application of the same software has been described by Pereira et al. [26], who studied the cracking behavior of cement paste, mortar, concrete, and fiber reinforced concrete. In the present study, the analysis was performed as a 2D analysis using photos taken with a 36.3 megapixel digital camera. The surface of the connection was spray painted with a white basis layer followed by random sprayed black dots to create a unique and recognizable pattern on the

surface. The area covered by the Aramis analysis corresponds approximately to the area of the joint, namely $L \cdot (b + 2d_k)$, see Figure 3. The results include the overall response of the shear connection, failure of the joint mortar between the precast elements, and also local failure of the shear keys. The results were dependent on the quality of the sprayed pattern, the light settings and the carefulness taken in the adjustment of the camera. The results did only cover the development of cracks on the surface of the joint, however the analysis provided invaluable information on the joint behavior during loading.

3.3. Test Results

Figure 4 presents the general characteristics of the load-displacement response of the different tested connections. The measured displacements are relative displacements (in the longitudinal direction of the connection) between the two precast elements. Figure 4(a) can be used as a direct comparison between series R and P, where the behavior of the reference specimens complies with previous investigations, e.g. described in details by Hansen et al. [4]. The first peak also appears to be the global peak, which is immediately followed by a softening branch as the shear displacement increases. It should be noted, that the response curve of specimen R1 represents a test where the U-bar loops are shoved away from each other whereas for specimens R2 and R3, the U-bars are shoved towards each other as the shear displacement increases. This indicates a very unfortunate property of the classical design because the post peak response apparently is dependent on the loading direction. It may very well be due to this matter, that the post peak behavior of the classical design in the literature is reported both as brittle and as ductile.

Figure 4(a) clearly illustrates the main difference between the two designs. The loads corresponding to the first peak are comparable for specimens having identical

A_s and identical key configuration. However, the post peak behavior differs significantly as the new design exhibits a pronounced ductile behavior. This ductile behavior is especially observed for the '2-on-2' connections, see Figure 4(b) which presents examples of the main findings of the test series I-IX. Before cracking, the joint behaves with a stiffness similar to that of a monolithic wall. At a relatively small load level, cracks at the interface between the joint mortar and the precast element develop, decreasing the stiffness slightly. At a higher load level diagonal cracks between the corners of each pair of opposite shear keys start to emerge on the surface, as indications of diagonal strut action. After diagonal cracking, the stiffness of the joint decreases until the first peak on the load-displacement curve is reached, which corresponds to the value of P_{FP} given in Table 1. For the new design, a drop in the response is observed after the first peak. However, as the displacement increases, the load increases again and reaches approximately the same level as the first peak. The relation between the first peak load and the ultimate load depends on the key design, which turns out to be one of the main parameters that control the failure mechanism. Rupture of the U-bars starts to take place at a displacement in the range of 12-20 mm, depending on the reinforcement configuration. The ultimate load of the joint, indicated as P_{U} in Table 1, is typically found at large displacements. The load level in Figure 4(b) is higher than the load level in Figure 4(a) due to the difference in the reinforcement area, A_s, per loop connection.

The first peak capacity, P_{FP}, is governed by several factors, as identified in the afore mentioned literature. In the present study, where the tensile capacity of the loop connections was designed to be governed by U-bar yielding, the magnitude of P_{FP} is influenced by the geometry of the shear keys. Generally a larger key area results in a higher first peak capacity. Specimen II2 has a smaller key area compared to V2 and VIII2. This explains the lower first peak capacity for II2, however, the response

after first peak shows the same tendencies as that of specimen VIII2 because both specimens had identical loop reinforcement configuration, see Figure 4(b). Furthermore, it is seen that the first peak capacities of V2 and VIII2 are rather similar as the key areas are identical. However, after the first peak, the two specimens behave differently as the governing failure mechanisms are different (referring to mechanism B and C introduced in Figure 7). The small key depth, d_k, of specimen V2 favors shearing of the key corners whereas the larger key depth of specimen VIII2 results in complete shearing of the key. These partly or complete key shearing failure mechanisms are in agreement with the findings for the classical keyed joint described by Hansen et al. [4]. Nimityongskul and Liu [9] also observed these failure mechanisms, and they interpreted the failure with partly shearing of the key corners as a consequence of an increase of the key area. A correlation between this failure mode and the depth of the shear keys has not been investigated until now.

3.4. Detection of Failure Mechanisms

As digital image correlation was used to monitor the cracking process on the surface of the specimen, the experimental failure mechanisms could be detected. For specimens with keys hidden in the joint, i.e. series I-IV where $h_k < t$, failure of the keys was only observed indirectly as displacements at the casting joint and as diagonal cracking in the joint mortar (see also Figure 9). For specimens with keys having $h_k = t$, cracking of the keyed area was clear and visible when occurring. Figure 5 shows an example of a complete shearing of a single key, where it is also observed that the preexisting diagonal crack closes almost completely as the key is sheared off. From the load-displacement response of the specimen, it appears that the observed first peak capacity was related to the shear failure of the keys. On this basis, it seems reasonable to conclude that failure of the shear keys also governs

the first peak capacity of the specimens with keys hidden in the joint ($h_k < t$). DIC measurements of the cracking/failure patterns have served as inspiration when developing collapse mechanisms used in the upper bound calculations of the first peak capacity, P_{FP}, (see Section 4).

3.5. Ductility of Connections

It appears from the test results that a much more ductile load-displacement response can be obtained by the new design as compared to the classical solution. To quantify the ductility of a shear joint, the concept of relative strain energy described by Engström [27] may be considered. Engström compared the maximum resistance to the average force, that can be resisted by the connection during the entire displacement spectrum. This results in an average-to-peak ratio less than or equal to unity, where unity is the ideal rigid-plastic behavior. In order to refine this measure, a ductility index as defined in Equation (1) is introduced:

$$D_I = \frac{1}{\delta_{\max} - \delta_{\mathrm{FP}}} \int_{\delta_{\mathrm{FP}}}^{\delta_{\max}} \frac{P(\delta)}{P_{\mathrm{FP}}} d\delta \tag{1}$$

The idea here is to evaluate the ability of the joint to dissipate energy in the displacement regime $\delta_{\mathrm{FP}} - \delta_{\max}$, where δ_{FP} corresponds to the shear displacement at the occurrence of the first peak capacity, while $\delta_{\max}$ is the maximum shear displacement capacity of the connection. The displacement capacity, $\delta_{\max}$, can e.g. be defined as the displacement where rupture of U-bars initiates or taken as a fixed predefined value. The index, D_I, is the ratio between the dissipated energy, see the filled area in Figure 6, and $P_{\mathrm{FP}} \cdot (\delta_{\max} - \delta_{\mathrm{FP}})$, which reflects the energy of a perfectly-plastic connection having the capacity P_{FP}, see the hatched area in Figure 6. The ductility index may attain a value larger than unity. An index $D_I > 1.0$ indicates that the joint has a robust behavior since it will be able to absorb the potential energy

released when e.g. gravitational loads (applied in a load controlled manner) reach the first peak capacity, P_{FP}. The ductility index is highly dependent on the total shear area of the keys, A_k, as the first peak capacity increases with increasing A_k. Table 1 contains calculated values of D_I for the tested joints. The maximum shear displacement is chosen as 13 mm for '2-on-1' connections and 20 mm for the '2-on-2' design as rupture of the reinforcement loops was observed around this magnitude of displacement. In general, the new design has a much higher D_I-index than the classical design. The most important factor for obtaining a high ductility index is the governing failure mechanism. For practical application, it should be noted that a mechanism with key corner shearing leads to the most ductile and robust response. This issue will be further addressed in Section 4.

4. Failure Mechanisms and Upper Bound Solutions

As demonstrated by the DIC analysis, see Section 3.4, the first peak load, P_{FP}, is governed by failure of the shear keys. In this paper, so-called first order rigid-plastic upper bound models will be developed to predict P_{FP}. The ultimate load, P_{U}, of the joints is associated with large displacements and cannot be modeled in the same simple manner. Analytical modeling of P_{U} would require second order plastic analyses with account for change of geometry. The theoretical treatment of P_{U} is not a part of this paper. In the following, concrete, mortar, and reinforcing steel are assumed to be rigid-perfectly plastic materials obeying the associated flow rule. Concrete and mortar are considered as Modified Coulomb materials with zero tensile strength. For plain strain problems, the energy dissipated per unit area of a failure surface (yield line) may be determined as follows [28, 29]:

$$W_A = \frac{1}{2}\nu f_c \left(1 - \sin\alpha\right) |\mathbf{u}|, \qquad \alpha \geq \varphi \tag{2}$$

Where α is the angle of the displacement vector with the yield line and φ is the internal angle of friction. The internal angle of friction is a material property, which depends partly on the aggregate sizes and partly on the aggregate content of the matrix [29]. Triaxial tests by Dahl [30] indicate that φ also depends on the confinement pressure. However, for normal strength concrete and low confinement pressures, the internal angle for friction is normally taken to be $\varphi = 37°$. For normal strength mortar with confinement pressures less than the uniaxial compressive strength of the mortar, Nielsen [31] reported tests indicating an internal angle of friction around 30°. In this study it is assumed that $\varphi = 30°$ for the mortar material used to grout the joints. As neither concrete nor mortar are perfectly plastic materials, an effectiveness factor ν is introduced into the theoretical solutions [29]. The ν-factor depends on the type of problem and is usually found by calibration with tests. For keyed joints transversely reinforced with high strength wire loops, Jørgensen and Hoang [23, 32] suggest to adopt a ν-formula similar to the one used for beam shear problems [33], but modified to the geometric layout of the keyed shear joint. Furthermore, the factor was adjusted to fit the shear capacity of joints cast with mortar. The ν-factor for mortar joints proposed by Jørgensen and Hoang is adopted in this work:

$$\nu = \frac{0.75}{\sqrt{f_c}} \left(1 + \frac{1}{\sqrt{L_k}} \right) \not> 1.0, \qquad (f_c \text{ in MPa}, \ L_k \text{ in m}) \tag{3}$$

It should be noted, that the dependency of ν on f_c and L_k basically reflects softening effects and size effects, which in the end is also due to softening. According to Equation (3), a decrease in key length will increase the effectiveness factor, which explains why identical key areas may lead to different tested load carrying capacities, depending on the L_k/h_k-ratio. In the test series I-IX the effectiveness factor ranges from 0.43 to 0.52.

4.1. Failure Mechanisms

The load carrying capacity, P_{cal}, related to a specific failure mechanism, is found by solving the work equation, in which the rate of work performed by the external loads must equal the rate of internal work dissipated in the yield lines. Figure 7 shows the three basic failure mechanisms A, B and C, considered in this study. The mechanisms have been identified partly on the basis of theoretical reasoning and partly with inspiration from the experimentally observed failure modes. For all three failure mechanisms it is assumed that the precast element on the right hand side experiences a rigid body motion described by the displacement vector $\mathbf{u}$:

$$\mathbf{u} = \begin{pmatrix} u_t \\ u_l \end{pmatrix} \tag{4}$$

The rate of external work is then given by:

$$W_E = P_{\text{cal}} u_l \tag{5}$$

For Mechanisms A and B, it is more convenient to express the components of $\mathbf{u}$ by $|\mathbf{u}|$ and the angle α as follows (see Figure 7):

$$u_l = |\mathbf{u}| \cos\alpha \tag{6}$$

$$u_t = |\mathbf{u}| \sin\alpha \tag{7}$$

The rate of internal work, W_I, for the three mechanisms may in general be written as:

$$W_I = W_{I,j}^c + W_I^s + W_I^{sL} \tag{8}$$

$$W_{I,j}^c = W_A A_j \tag{9}$$

$$W_I^s = A_s f_y u_t \tag{10}$$

$$W_I^{sL} = A_{sL} f_{yL} u_l \tag{11}$$

where $W_{I,j}^{c}$ is the contribution from a concrete/mortar yield line with the area A_j, W_I^s is the contribution from the U-bars and W_I^{sL} is the contribution from the locking bar. Yielding of the locking bar is only required in Mechanism B.

For a general description the following parameters are introduced and explained in Table 3:

$$A_k = L_k h_k, \quad A_d = t\sqrt{b^2 + L_k^2}, \quad A_i = h_k \frac{d_k}{\sin\gamma},$$
$$\tan\beta = \frac{b}{L_k}, \quad \Phi = \frac{n+1}{n}\frac{A_s f_y}{A_k f_c}, \quad \Phi_L = \frac{A_{sL} f_{yL}}{n A_k f_c}$$

The parameters introduced make it easier to derive general formulas for calculation of a joint with n shear keys and $(n+1)$ pairs of U-bar loops crossing the joint interface. It is convenient to define the shear capacity of the joint by an average shear stress, τ, which is related to the total area of the shear keys:

$$\frac{\tau}{\nu f_c} = \frac{P_{\text{cal}}}{n A_k \nu f_c} \tag{12}$$

4.2. Mechanism A - Key cut off

To solve the work equation for Mechanism A, the rate of internal work is found as the sum of contributions from n shear keys being sheared off (using $A_j = A_k$) and the contribution from $(n+1)$ reinforcement loops stressed to yielding:

$$W_I = n\frac{1}{2}\nu f_c \left(1 - \sin\alpha\right) A_k |\mathbf{u}| + (n+1)\, A_s f_y u_t \tag{13}$$

An upper bound solution is established from $W_E = W_I$:

$$\frac{\tau}{\nu f_c} = \frac{1 - \sin\alpha}{2\cos\alpha} + \frac{\Phi}{\nu}\tan\alpha \tag{14}$$

The optimal solution is found by minimizing the expression with respect to the angle of displacement, α. The optimal solution is found when:

$$\alpha = \arcsin\left(1 - \frac{2\Phi}{\nu}\right), \qquad \alpha \geq \varphi \tag{15}$$

From Equation (15) it is implicitly given that the key area influences the optimal angle of displacement and thereby the capacity of the shear connection. It should be noted that the expression, with only slight change of notation, is similar to the findings of [19] and [22].

4.3. Mechanism B - One diagonal yield line

For Mechanism B, the rate of internal work consists of the following contributions: $(n-1)$ times $W^c_{I,j}$ with $A_j = A_k$; one times $W^c_{I,j}$ with $A_j = A_d$; $(n+1)$ reinforcement loops stressed to yielding, and one contribution from the locking bar stressed to yielding. The upper bound solution is found to be:

$$\frac{\tau}{\nu f_c} = \frac{n-1}{2n}\frac{1-\sin\alpha}{\cos\alpha} + \frac{A_d}{2nA_k}\frac{1-\sin\left(\beta+\alpha\right)}{\cos\alpha} + \frac{\Phi}{\nu}\tan\alpha + \frac{\Phi_L}{\nu} \tag{16}$$

Which has a minimum when the angle of displacement is:

$$\alpha = \arcsin\left(\frac{n-1+\dfrac{t}{h_k}-2n\dfrac{\Phi}{\nu}}{n-1+\dfrac{A_d}{A_k}}\right), \qquad \alpha \geq \varphi \tag{17}$$

From Equation (17) it can be seen that the ratio between the height of the key and the thickness of the connection influences the optimal solution for this particular failure mechanism.

4.4. Mechanism C - Inclined key cut off

For mechanism C, the rate of internal work is found as n times $W^c_{I,j}$ (with $A_j = A_i$) plus the contribution from $(n+1)$ reinforcement loops. In this mechanism the angle between the l-axis and the inclined yield line is γ, see Figure 7(c). The components of the displacement vector are given by:

$$u_l = |\mathbf{u}|\cos\left(\gamma+\alpha\right) \tag{18}$$

$$u_t = |\mathbf{u}|\sin\left(\gamma+\alpha\right) \tag{19}$$

As the relation between the transverse and the longitudinal displacement is dependent on the sum of γ and α, the lower limit of the condition $\alpha \geq \varphi$ is reached at lower reinforcement degrees for this mechanism compared to Mechanisms A and B. Therefore (and to simplify) it is for this particular mechanism assumed that $\alpha = \varphi = 30°$. The optimization of the upper bound solution is then reduced to an optimization problem involving only the angle γ, which is governed by the key dimensions and the internal angle of friction φ. The load carrying capacity is given by:

$$\frac{\tau}{\nu f_c} = \frac{d_k}{2L_k} \frac{1 - \sin\varphi}{\sin\gamma\cos(\gamma + \varphi)} + \frac{\Phi}{\nu}\tan(\gamma + \varphi) \tag{20}$$

The critical angle of the inclined yield line is found as:

$$\gamma = \arctan\left(\frac{\cos\varphi}{\sin\varphi + \sqrt{1 + \frac{\Phi}{\nu}\frac{2L_k}{d_k}\frac{\cos\varphi}{1 - \sin\varphi}}}\right) \tag{21}$$

It appears that the internal angle of friction of the joint mortar influences the capacity significantly and to a large extent dictates, in combination with the key length to depth ratio (L_k/d_k), which of the failure mechanisms (A, B or C) that constitutes the critical mechanism.

5. Influence of Key Geometry on Failure Mode

From the derived expressions for the load carrying capacity (Equations (14), (16), and (20)) and the corresponding optimal angles of displacement, it is evident that the geometry of the joint, and in particular the geometry of the keys, play an important role in defining the governing failure mechanism. Figure 8 contains the results of a theoretical comparison of the load carrying capacity related to the three basic failure mechanisms. The calculations have been performed by assuming a reinforcement

arrangement similar to the one used in the experimental program series I-IX. Figure 8(a) demonstrates the influence of the key height, h_k, and it appears that a higher relative key height, h_k/t, favors Mechanism B compared to a small relative key height which favors Mechanism A. Figure 8(b) demonstrates the influence of the key depth on the failure mechanism of a joint configuration similar to the test specimens of Series V to IX, where the relative key height $h_k/t = 1$. As expected, the smaller key depths favor Mechanism C.

The transition point (in Figure 8(b)) between the failure mechanisms is of particular interest because the deformation characteristics of the joint depends on the governing failure mechanism. As shown in Figure 4(b), shearing of the key corners (specimen VII) results in a pronounced ductile behavior, which in turns leads to a high ductility index. In this context it should be noted, that the internal angle of friction for mortar is of significant interest because the transition point, see Figure 8(b), partly depends on the magnitude of φ. Aramis recordings of the relative displacements at the first peak load indicate that $\varphi = 30°$ is an appropriate choice for the material used in this study and, furthermore, it is in accordance with the investigations by Nielsen [31]. The recorded relative displacements were compared to the theoretical relative displacements for test specimens where the angle of displacement was predicted to be $\alpha = \varphi$.

6. Failure Mechanisms based on Experimental Observations

Based on the experimental observations, the theoretical failure mechanisms for Series I-IX are evaluated. DIC-measurements have shown, that a failure mechanism similar to Mechanism B, but with a relatively large crack opening in one diagonal crack prior to the first peak load, governs independently of the height of the key. Figure 9 shows Aramis recordings of the cracking process of specimen III2, which

according to the theoretical calculations should reach the first peak load carrying capacity by development of Mechanism A. It appears that diagonal cracks develop even before first peak, see Figure 9(a), and the relative displacements during failure take place in one of the existing diagonal cracks, see development from Figure 9(b) to Figure 9(c). The crack opening of the diagonal cracks prior to first peak can be determined from Aramis measurements. Figure 10 shows examples of recorded crack opening of the largest diagonal crack (only crack opening in the longitudinal direction of the joint is shown). It appears that the crack opening before first peak load, P_{FP}, is approximately 0.4 mm, which is relatively large for mortar. This observation leads to the conclusion that the dissipation in the diagonal yield line (i.e. the mortar contribution) must be significantly reduced and thereby making a mechanism which is similar to Mechanism B more critical than mechanism A.

In the following, two additional failure mechanisms are introduced, namely Mechanism D similar to Mechanism B, see Figure 7(b), but omitting the mortar contribution from the diagonal yield line when calculating the rate of internal work, and Mechanism E based on Mechanism C, however, introducing a diagonal yield line, see Figure 11, and omitting the mortar contribution from the diagonal yield line in the calculation. For both cases the contribution from the longitudinal locking bar is considered.

In practice, the length of a shear wall connection will at least be equal to the height of one storey and for this reason, there will be many more shear keys in these connections as compared to the connections investigated in this study. When many shear keys are present, the significance of Mechanisms D and E will be limited. However, for the limited geometry of the test specimens, the influence of the boundary effect included in these mechanisms is relevant. The load carrying capacity of

Mechanism D is found to be:

$$\frac{\tau}{\nu f_c} = \frac{n-1}{2n}\frac{1-\sin\alpha}{\cos\alpha} + \frac{\Phi}{\nu}\tan\alpha + \frac{\Phi_L}{\nu} \tag{22}$$

The optimal angle of displacement is given as:

$$\alpha = \arcsin\left(1 - \frac{2n\Phi}{(n-1)\,\nu}\right), \qquad \alpha \geq \varphi \tag{23}$$

For Mechanism E, see Figure 11, the load carrying capacity, assuming $\alpha = \varphi$, is:

$$\frac{\tau}{\nu f_c} = \frac{n-1}{2n}\frac{d_k}{L_k}\frac{1-\sin\varphi}{\sin\gamma\cos(\gamma+\varphi)} + \frac{\Phi}{\nu}\tan(\gamma+\varphi) + \frac{\Phi_L}{\nu} \tag{24}$$

The critical angle, γ, of the inclined yield line in the keys is found as:

$$\gamma = \arctan\left(\frac{\cos\varphi}{\sin\varphi + \sqrt{1 + \dfrac{n}{(n-1)}\dfrac{\Phi}{\nu}\dfrac{2L_k}{d_k}\dfrac{\cos\varphi}{1-\sin\varphi}}}\right) \tag{25}$$

It should be noted, that Mechanisms B/D and E are only relevant for test Series I-IV where the specimens had '2-on-2' loop connections. For specimens in Series P with '2-on-1' connections, the asymmetric reinforcement arrangement favors Mechanism A or C. This can be seen in Figure 12, where Aramis recordings show that no diagonal cracks were present just after the first peak load.

7. Comparison of Tests with Theory

Table 4 contains the obtained experimental first peak loads as well as the theoretical determined values. For test specimens in Series I-IX, the theoretical capacity has been determined as the minimum value predicted from the five presented failure mechanisms. For specimens in Series P only Mechanism A and C are of interest. The yield strength of the reinforcement loops in Series P was $f_y = 509$ MPa, the

width of the joint was $b = 80$ mm, and the remaining properties are given in Table 1 and 2.

Figure 13 and 14 contain a graphical comparison where the governing failure mechanisms are identified. The calculations are performed using the average compression strength of the grout mortar and the reinforcement strengths given in Table 2. Figure 13 contains a comparison where the length of the shear keys, L_k, is varied and the thickness is kept constant at half the panel thickness. The results thereby compares to Series I-IV (Mechanism C is not critical). Figure 14 contains the comparison for varying key depths with constant key area, i.e. a comparison for Series V-IX. It can be seen that the refined Mechanism D captures the behavior and predicts the load carrying capacity of the specimens with large key depths. It can also be seen that Mechanism E explains the cracking behavior of the specimens with small key depths before Mechanism D becomes the governing mechanism for larger key depths. Table 4 also contains a summary of the observed as well as predicted failure mechanisms. If a failure mode including a diagonal crack was observed, the failure is regarded as B for the key cut off and E for the inclined key cut off. Mechanism D cannot be observed experimentally, but in fact an observed Mechanism B might relate to a theoretical Mechanism D. It can be seen from Table 4 that both Mechanism B and E were observed in test series VI. It should be noted that a smaller value of φ changes the transition point towards a larger key depth. However, an in-depth study of the internal angle of friction for mortar is needed to clarify the property and perhaps also the validity of the normality condition for mortar materials.

In Figure 13 the key area is presented as the ratio between the area of a single key compared to the joint area, A_t. The joint area is calculated using the center distance of the reinforcement loops, given as s in Figure 3, and the height of the specimen, t. It can be seen that the average shear stress can be higher for a smaller relative

key area, as expected considering softening effects in the mortar material. Generally, good agreement is found between the test results and the calculations. In Figure 13 and 14, the capacity as predicted by the Eurocode 2 formula has been included as well. It is clearly seen that the empirical formula of Eurocode 2 is too conservative when applied to the new connection design. In this context it should be noted that the Eurocode 2 method does not take into account the specific key geometry.

8. Conclusion

A new and construction-friendly loop connection for the assembly of precast shear wall panels has been developed and tested. The structural performance of the new connection, in terms of ductility, is superior to that of the classical design. A ductility index has been introduced in order to evaluate and compare the performance of the developed design to that of the classical design. For the tested designs, the first peak on the response curve has been identified as the load that causes failure of the shear keys. Theoretical failure mechanisms have been established and used to derive upper bound plasticity solutions to calculate the first peak capacity. The failure mechanisms for the tested connections have been refined based on observations from the experiments and the results of DIC analysis.

The significance of the key dimensions has been addressed and the influence of the key height and depth on the failure mode has been outlined. The developed models predict the transition point between the two main failure mechanisms, in terms of key depth: complete key cut off or inclined key cut off, see Figure 14. The refined Mechanisms D and E, relevant for the limited geometry tested, captured and explained the experimental observations. For design of longer connections as those found in practice, the theoretical basic mechanisms A, B and C presented in Figure 7 will be sufficient.

It can be concluded that the new connection design is a feasible and promising practical solution that should be subjected to further investigation with the perspective of replacing the classical solution. To mature the new design for practical use, it is necessary to clarify a number of issues, including:

- Detailed characterization of the properties of grout mortar
- Test of a wider range of U-bar diameters and possibly a variation of the geometry of the U-bars
- Test of the tensile capacity of the connection
- Test of anchorage properties of the lacer reinforcement
- Investigation and modeling of the increase in load carrying capacity after first peak

Acknowledgment

The experimental program was financially supported by the Danish Association for Precast Concrete Elements and the COWI Foundation. The test elements were produced at CRH Concrete and the experimental work was conducted with support from students at DTU Civil Engineering. B.Eng. Rune Pedersen and B.Eng. Mads Herløv contributed with test Series R and P in their bachelor thesis, M.Sc. J. Svejgaard contributed with test Series I-IV, and M.Sc. L. Øvrelid contributed with test Series V-IX in their master theses. Finally, the use of double headed studs as lacer bars instead of conventional stirrups was suggested by PhD Tim Gudmand-Høyer. The authors gratefully acknowledge these valuable contributions.

References

[1] K. K. B. Dahl, Bella Sky Hotel - taking precast concrete to the limit, Struct. Concr. 15 (4) (2014) 441–447.

[2] K. Flindt Jørgensen, Bella Sky Hotel - exploring the potential in precast concrete design, Struct. Concr. 16 (4) (2015) 449–457.

[3] Fib, Bulletin 43: Structural connections for precast concrete buildings, federation international du béton, 2008.

[4] K. Hansen, M. Kavyrchine, G. Melhorn, S. Ø. Olesen, D. Pume, H. Schwing, Keyed shear joints - SBI rapport 97, Tech. rep., Danish Building Research Institute (1976).

[5] R. Halasz, G. Tantow, Schubfestigkeit der Vertikalfugen im Grosstafelbau, in: Berichte aus der Bauforschung, H. 39, Verlag Wilhelm Ernst & Sohn. Berlin, 1966.

[6] A. Cholewicki, Loadbearing Capacity and Deformability of Vertical Joints in Structural Walls of Large Panel Buildings, Build. Sci. 6 (9) (1971) 163–184.

[7] M. Pommeret, Le comportement sous charges ou déformations répétées alternées des joints verticaux entre panneaux préfabriqués, Tech. rep., Centre expérimental de recherches et d'études du bastiment et des travaux publics, Saint Remy les Chevreuxe (1972).

[8] J. Fauchart, P. Cortini, Étude expérimentale de joints horizonraux entre panneaux préfabriqués pour murs de batiments, Annales de L'institut Technique du Batiment et Des Travaux Publics, 1972.

[9] P. Nimityongskul, H. Y. Liu, Vertical Shear Strength of Joints in Prefabricated Loadbearing Walls, Hous. Sci. 4 (2) (1980) 137–157.

[10] S. C. Chakrabarti, N. N. Bhise, K. N. Sharma, Failure Criterion of Vertical Shear Key Joints in Prefabricated Wall Panels, Indian Concr. J. 55 (3) (1981) 63–67.

[11] H. M. Abdul-Wahab, An Experimental Investigation of Vertical Castellated Joints between Large Concrete Panels, Struct. Eng. 64B (4) (1986) 93–99.

[12] R. L. Serrette, S. Rizkalla, J. Heuvel, Multiple Shear Key Connections for Loadbearing Shear Wall Panels, PCI J. 34 (2) (1989) 104–120.

[13] N. Rossley, F. N. A. A. Aziz, H. C. Chew, N. Farzadnia, Behaviour of Vertical Loop Bar Connection in Precast Wall Subjected To Shear Load, Aust. J. Basic Appl. Sci. 8 (1) (2014) 370–380.

[14] R. Vaghei, F. Hejazi, H. Taheri, M. S. Jaafar, A. A. A. Ali, Evaluate Performance of Precast Concrete Wall to Wall Connection, APCBEE Procedia 9 (Icbee 2013) (2014) 285–290.

[15] CEN, EN1992-1-1 Eurocode 2: Design of concrete structures – Part 1-1: General rules and rules for buildings, 3rd Edition, European Committee for Standardization, 2004.

[16] Y. Kaneko, J. J. Connor, T. C. Triantafillou, C. K. Leung, Fracture Mechanics Approach for Failure of Concrete Shear Keys. I: Theory, J. Eng. Mech. 119 (4) (1993) 681–700.

[17] Y. Kaneko, J. J. Connor, T. C. Triantafillou, C. K. Leung, Fracture Mechanics Approach for Failure of Concrete Shear Keys. II: Verification, J. Eng. Mech. 119 (4) (1993) 701–719.

[18] B. Y. Kaneko, H. Mihashi, Analytical study on the cracking transition of concrete shear key, Mater. Struct. 32 (April) (1999) 196–202.

[19] B. C. Jensen, On the Ultimate Load of Vertical, Keyed Shear Joints in Large Panel Buildings, Tech. rep., Institute of Building Design, Technical University of Denmark (1975).

[20] S. C. Chakrabarti, G. C. Nayak, D. K. Paul, Shear Characteristics of Cast-in-Place Vertical Joints in Story-High Precast Wall Assembly, ACI Struct. J. 85 (1) (1988) 30–45.

[21] H. M. Abdul-Wahab, S. Y. H. Sarsam, Prediction of Ultimate Shear Strength of Vertical Joints in Large Panel Structures, ACI Struct. J. 88 (2) (1991) 204–213.

[22] J. Christoffersen, Ultimate Capacity of Joints in Precast Large Panel Concrete Buldings, Series R No 25, Ph.D. thesis, Technical Universioty of Denmark, Department of Structural Engineering and Materials, Lyngby (1997).

[23] H. B. Jørgensen, L. C. Hoang, Load Carrying Capacity of Keyed Joints Reinforced with High Strength Wire Rope Loops, in: Concr. - Innov. Des. fib Symp. Copenhagen, 2015, pp. 1–13.

[24] H. B. Jørgensen, L. C. Hoang, Tests and limit analysis of loop connections between precast concrete elements loaded in tension, Eng. Struct. 52 (2013) 558–569.

[25] GOM, Aramis User Manual - Software v6.1 and higher, GOM Optical Measuring Techniques, Braunschweig, Germany, 2009.

[26] E. B. Pereira, G. Fischer, J. A. O. Barros, Image-based Detection and Analysis of Crack Propagation in Cementitious Composites, in: C. Leung, K. T. Wan (Eds.), Proc. Int. RILEM Conf. Adv. Constr. Mater. Through Sci. Eng., Hong Kong, China, 2011, pp. 1–8.

[27] Björn Engström, Ductility of Tie Connections in Precast Structures, Ph.D. thesis, Chalmers University of Technology, Göteborg (1992).

[28] B. C. Jensen, Nogle Plasticitetsteoretiske Beregninger af Beton og Jernbeton (English: Some Applications of Plastic Analysis to Plain and Reinforced Concrete), Report 111, Ph.D. thesis, Technical University of Denmark, Copenhagen (1976).

[29] M. P. Nielsen, L. C. Hoang, Limit Analysis and Concrete Plasticity, 3rd Edition, CRC Press, Taylor & Francis Group, 2011.

[30] K. K. B. Dahl, A Failure Criterion for normal and High Strength Concrete, Tech. rep., Technical University of Denmark, Lyngby (1992).

[31] C. V. Nielsen, Triaxial Behavior of High-Strength Concrete and Mortar, ACI Mater. J. 95 (2) (1998) 144–151.

[32] H. B. Jørgensen, Strength of Loop Connections between Precast Concrete Elements, Ph.D. thesis, University of Southern Denmark, Department of Technnology and Innovation (2014).

[33] J.-P. Zhang, Diagonal cracking and shear strength of reinforced concrete beams, Mag. Concr. Res. 49 (178) (1997) 55–65.

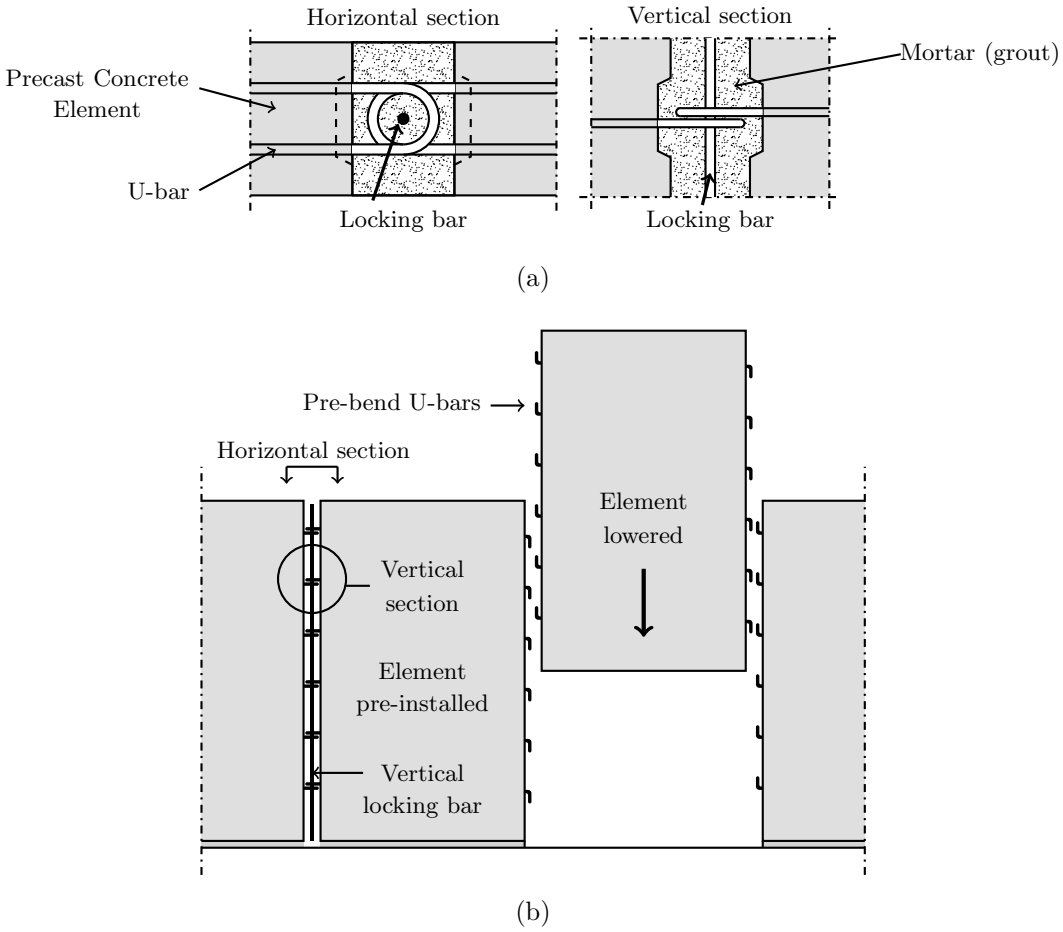

Figure 1: *(a) Classical shear connection design and (b) illustration of procedure for assembling of precast elements*

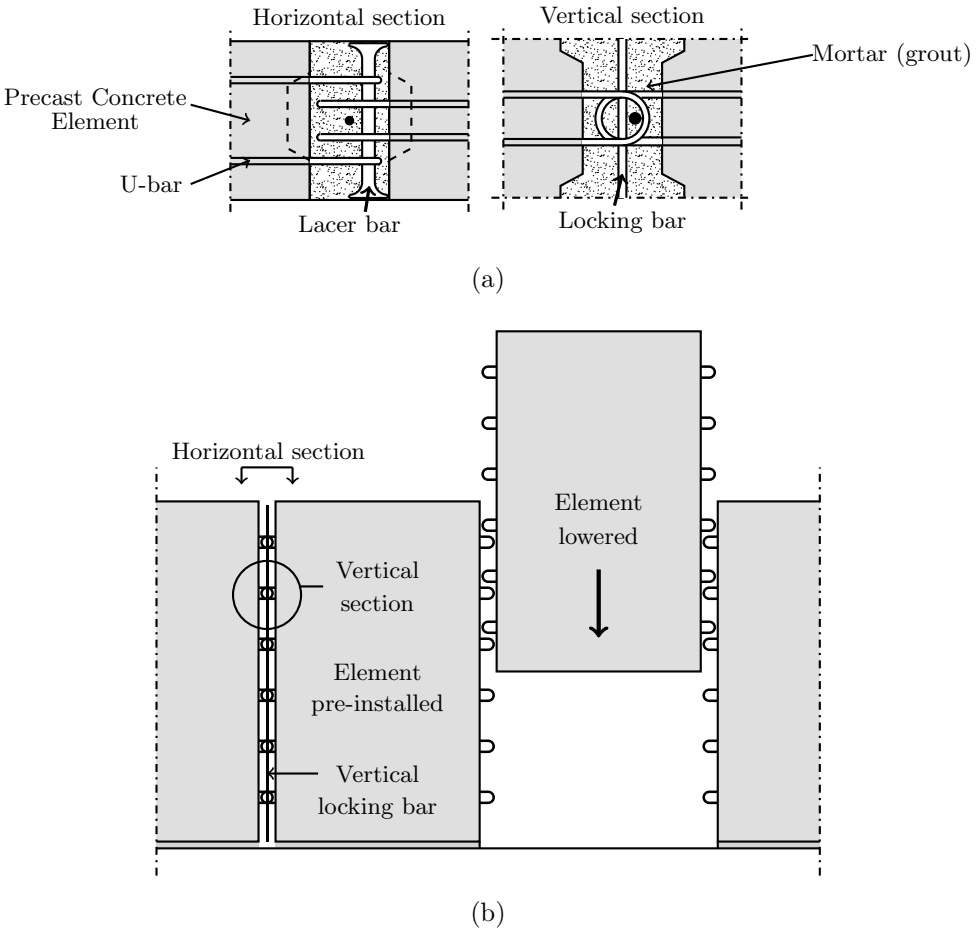

Figure 2: *(a) New construction-friendly connection design and (b) illustration of procedure for assembling of precast elements*

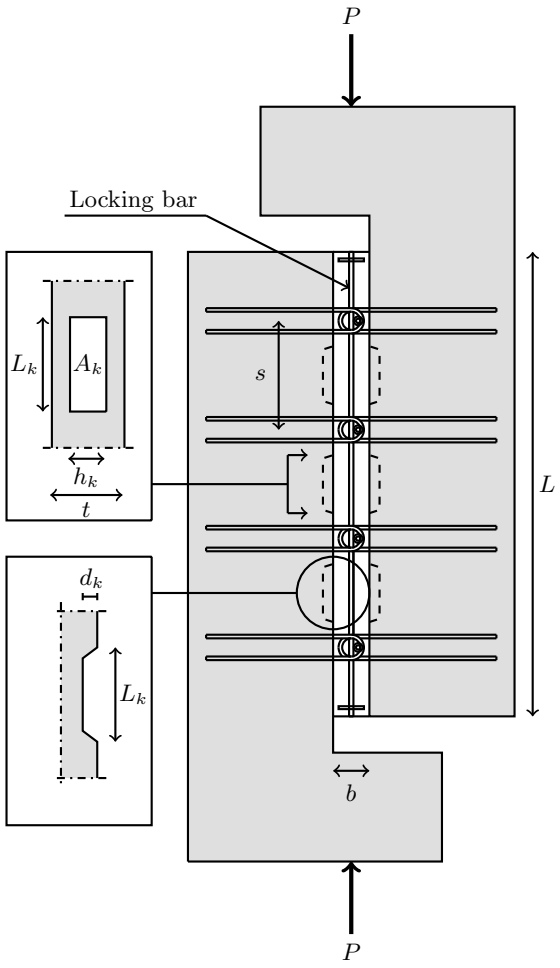

Figure 3: *General layout of push-off test specimens, thickness equals 200 mm (reinforcement in precast element not shown)*

Table 1: *Geometrical parameters and strength properties of the joints in the experimental program*

	No.	$f_c^\star$ [MPa]	h_k [mm]	L_k [mm]	A_k [mm^2]	d_k [mm]	A_s [mm^2]	P_{FP} [kN]	P_{U} [kN]	D_I
R	1	34.6	85	160	13600	16	**101**	282.43	-	0.42*
	2	35.7	85	160	13600	16	**101**	303.80	-	0.59*
	3	35.7	85	160	13600	16	**101**	337.42	-	0.70*
P	1	38.1	85	160	13600	16	**101**	344.24	357.45	1.00*
	2	38.1	85	160	13600	16	**101**	347.04	368.12	0.97*
	3	42.7	85	160	13600	16	**101**	342.49	339.97	0.87*
	4	42.7	85	160	13600	16	**101**	331.42	324.49	0.95*
I	1	31.2	100	**120**	12000	28	201	379.02	441.21	1.03†
	2	34.2	100	**120**	12000	28	201	416.59	472.92	1.00†
II	1	31.2	100	**140**	14000	28	201	366.40	463.78	1.06†
	2	34.2	100	**140**	14000	28	201	414.46	462.48	1.00†
III	1	31.2	100	**160**	16000	28	201	393.04	494.70	1.07†
	2	34.2	100	**160**	16000	28	201	473.52	514.87	0.98†
IV	1	31.2	100	**180**	18000	28	201	439.44	470.89	0.94†
	2	34.2	100	**180**	18000	28	201	478.17	515.31	0.96†
V	1	31.2	200	140	28000	**10**	201	475.24	488.97	0.97†
	2	34.2	200	140	28000	**10**	201	492.86	535.61	1.04†
VI	1	30.6	200	140	28000	**16**	201	527.09	502.55	0.89†
	2	30.6	200	140	28000	**16**	201	523.82	550.98	0.90†
VII	1	30.6	200	140	28000	**20**	201	549.17	451.58	0.78†
	2	30.6	200	140	28000	**20**	201	524.46	527.85	0.87†
VIII	1	30.6	200	140	28000	**25**	201	507.05	528.67	0.92†
	2	30.6	200	140	28000	**25**	201	516.97	545.33	0.92†
IX	1	30.6	200	140	28000	**28**	201	526.53	534.19	0.93†
	2	30.6	200	140	28000	**28**	201	527.59	527.07	0.88†

* Compression strength of mortar

* Using $\delta_{max} = 13\ mm$

† Using $\delta_{max} = 20\ mm$

Table 2: *Parameters kept constant for series I-IX*

Description	Symbol	Value
U-bar diameter	ϕ	8 mm
Yield strength of U-bar	f_y	487 MPa
Lacer bar diameter	ϕ_{Lacer}	16 mm
Yield strength of lacer bar	$f_{y,Lacer}$	563 MPa
Diameter of locking bar	ϕ_L	12 mm
Yield strength of locking bar	f_{yL}	584 MPa
Panel thickness	t	200 mm
Internal bend diameter of loops	D	60 mm
Width of joint	b	100 mm
Distance between loops	s	300 mm
Total length of joint	L	1280 mm
Strength of precast panels	$f_{c,element}$	49.6 MPa
Max aggregate size in mortar	d_{max}	4 mm

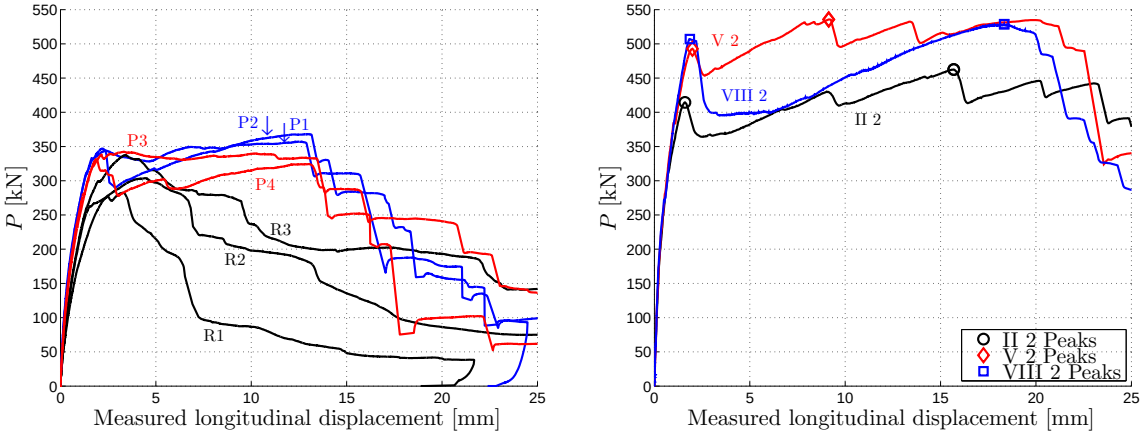

(a) *Comparison of series R to series P* (b) *Load-displacement curves for the new design*

Figure 4: *Examples of performance of tested shear keyed joints*

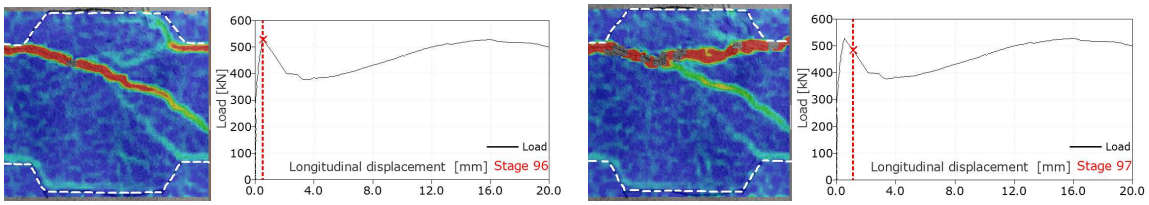

(a) *At first peak load,* P_{FP} (b) *Just after first peak load,* P_{FP}

Figure 5: *Example of complete key shearing (keys indicates with dashed line) at first peak load,* P_{FP}*, specimen IX2,* $d_k = 28$ *mm.*

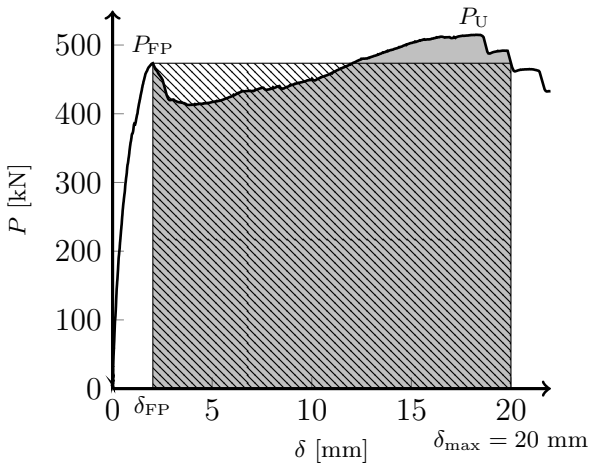

Figure 6: *Example of calculation of the ductility index,* D_I*, for specimen III2,* $D_I = 0.98$

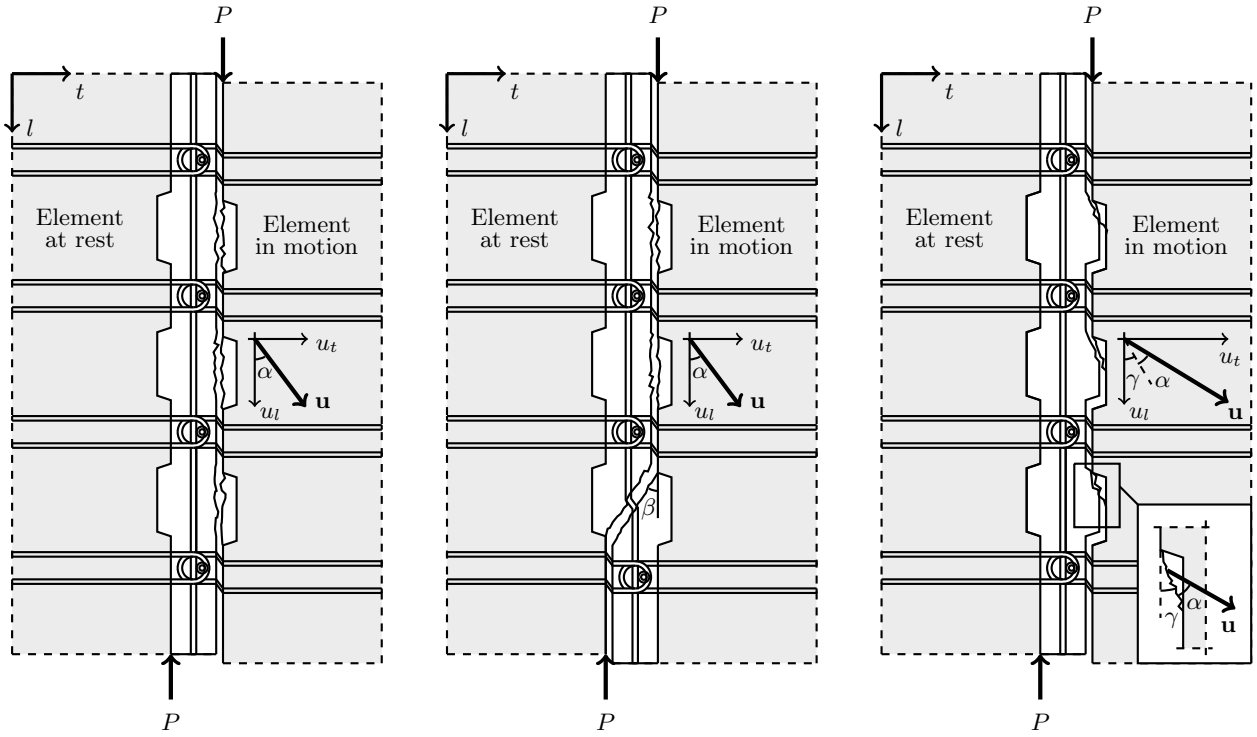

(a) *Mechanism A - Key cut off*

(b) *Mechanism B(D) - One diagonal yield line*

(c) *Mechanism C - Inclined key cut off*

Figure 7: *Basic failure mechanisms*

Table 3: *Symbols used in the theoretical determination of the first peak capacity*

Symbol	Definition
A_s	Reinforcement area per loop connection $4\frac{\pi}{4}\phi^2$ for 2-on-2 connections $2\frac{\pi}{4}\phi^2$ for 2-on-1 connections
A_k	Area of one shear key
A_d	Area of diagonal yield line
A_i	Area of inclined yield line in a shear key
Φ	Reinforcement degree of loop connection
Φ_L	Reinforcement degree of locking bar
β	Slope of diagonal yield line
γ	Slope of inclined yield line in a shear key

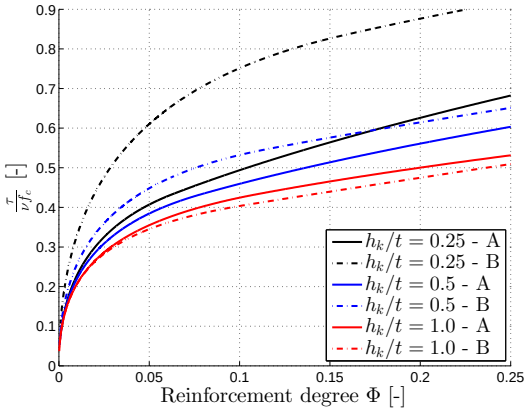

(a) *Load carrying capacity for varying relative height of key,* h_k/t, $f_c = 31$ *MPa*

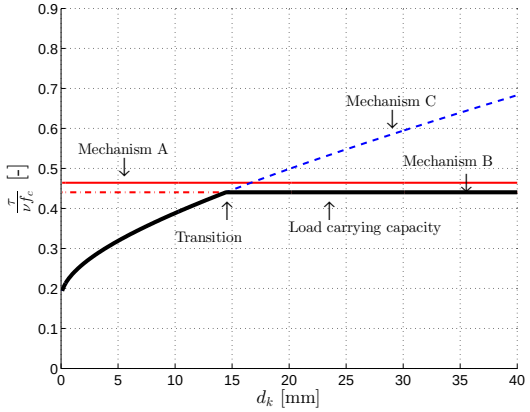

(b) *Load carrying capacity for varying key depth,* $f_c = 31$ *MPa,* $L_k = 0.140$ *m,* $h_k = 0.200$ *m,* $\Phi = 0.15$

Figure 8: *Illustrations of change in failure mechanism when changing geometry of the shear keys*

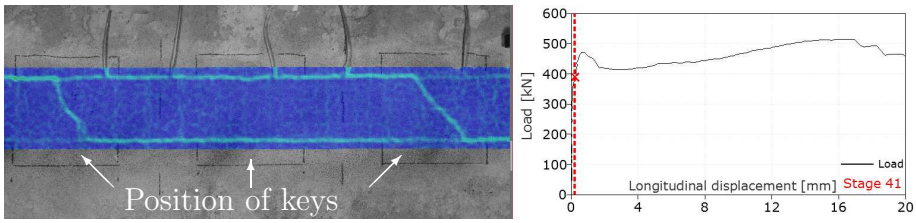

(a) *Major principal strain at first diagonal cracking*

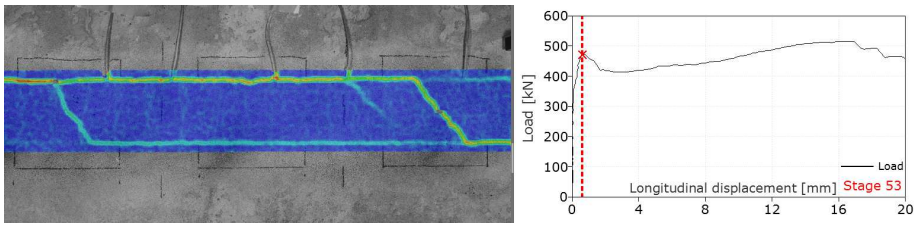

(b) *Major principal strain at first peak load*

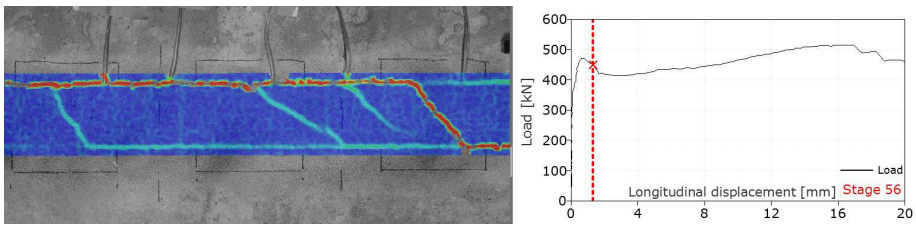

(c) *Major principal strain just after first peak*

Figure 9: *Aramis record of strain localization and cracking behavior of shear connection around first peak load, specimen III2*

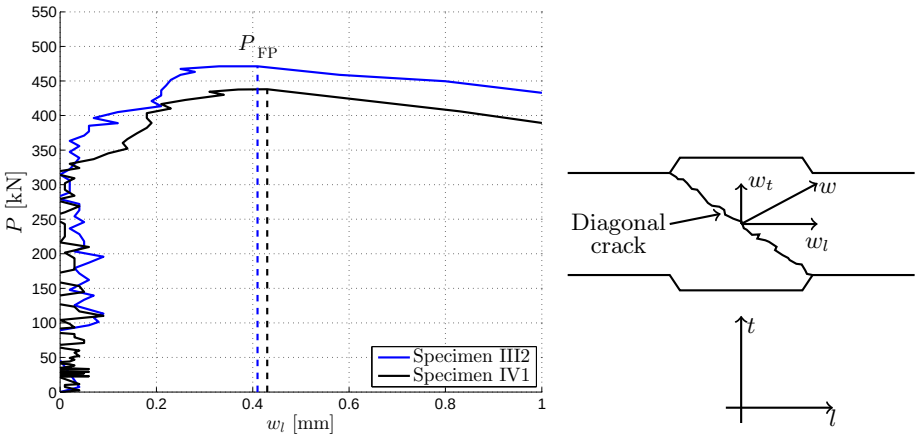

(a) (b)

Figure 10: *(a) Measured longitudinal crack opening in diagonal crack between shear keys and (b) definition of crack opening*

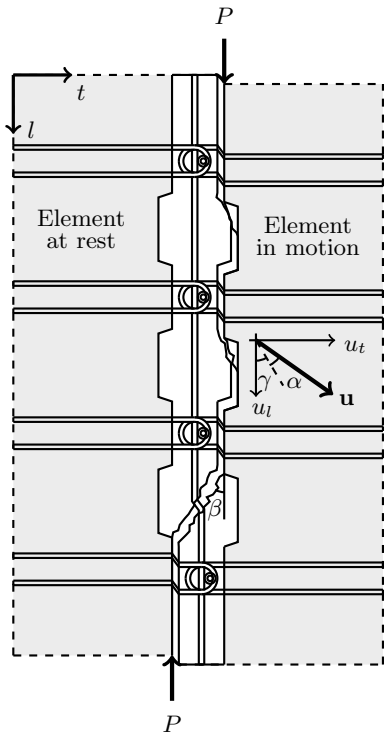

Figure 11: *Mechanism E, based on experimental observations*

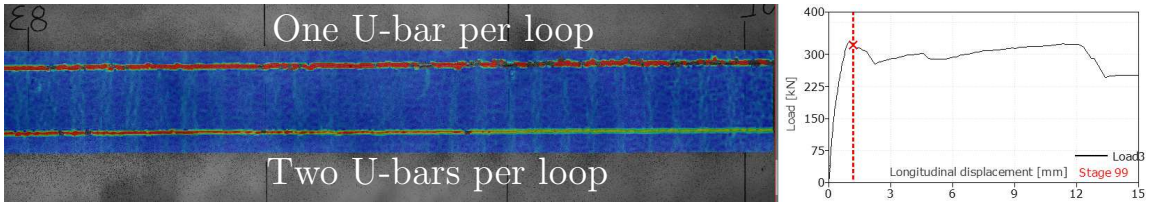

Figure 12: *Major principal strain distribution just after first peak load, P_{PF}, of '2-on-1' specimen (specimen P4) from pilot test series*

Table 4: *Comparison of test results with theoretical values*

	No.	P_{FP} [kN]	P_{cal} [kN]	$\frac{P_{\mathrm{FP}}}{P_{\mathrm{cal}}}$ [-]	Failure Mechanism Obs./Pre.
P	1	344.24	291.12	1.18	C/C
	2	347.04	291.12	1.19	C/C
	3	342.49	297.16	1.15	C/C
	4	331.42	297.16	1.12	C/C
I	1	379.02	395.34	0.96	B/A
	2	416.59	403.29	1.03	B/A
II	1	366.40	412.67	0.89	B/A
	2	414.46	421.43	0.98	B/A
III	1	393.04	427.62	0.92	B/D
	2	473.52	433.99	1.09	B/D
IV	1	439.44	438.33	1.00	B/D
	2	478.17	455.20	1.07	B/D
V	1	475.24	500.73	0.95	E/E
	2	492.86	508.21	0.97	E/E
VI	1	527.09	538.50	0.98	E/D
	2	523.82	538.50	0.97	B/D
VII	1	549.17	538.50	1.02	B/D
	2	524.46	538.50	0.97	B/D
VIII	1	507.05	538.50	0.94	B/D
	2	516.97	538.50	0.96	B/D
IX	1	526.53	538.50	0.98	B/D
	2	527.59	538.50	0.98	B/D
Mean				1.01	
Standard deviation				0.08	

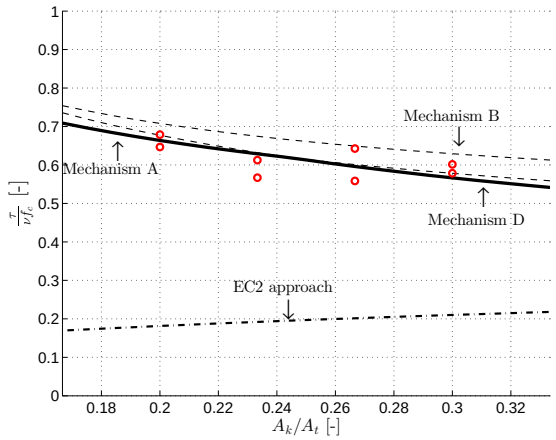

Figure 13: *Comparison of theory with results for series I-IV,* $f_{c,average} = 33.0$ *MPa*

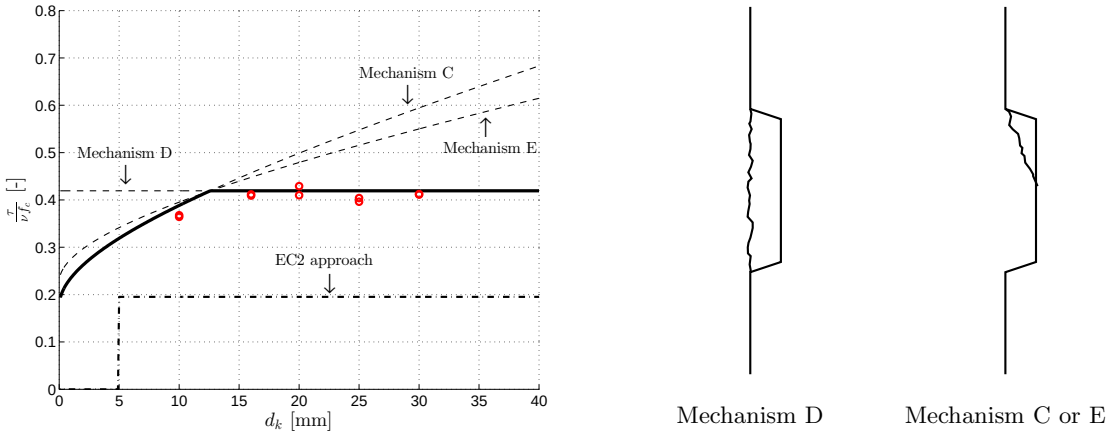

(a) (b)

Figure 14: *(a) Comparison of theory with results for series V-IX,* $f_{c,average} = 31.0$ *MPa, and (b) main failure modes*

Notation

A_d	Area of diagonal yield line	α	Angle of displacement vector
A_i	Area of inclined yield line in a shear key	β	Slope of diagonal yield line
A_j	Area of yield line	δ	Longitudinal displacement
A_k	Area of one shear key	δ_{max}	Displacement capacity
A_s	Reinforcement area per loop	δ_{FP}	Displacement at first peak
A_{sL}	Reinforcement area of locking bar	γ	Slope of inclined yield line in a shear key
A_t	Area of joint	ϕ	U-bar diameter
b	Width of joint	ϕ_{Lacer}	Lacer bar diameter
D	Internal bend diameter of loops	ϕ_L	Locking bar diameter
D_I	Ductility index	φ	Internal angle of friction
d_k	Depth of shear key	Φ	Reinforcement degree of loop connection
d_{max}	Maximum aggregate size in mortar	Φ_L	Reinforcement degree of locking bar
f_c	Compression strength	ν	Effectiveness factor
f_y	Yield strength of U-bar	τ	Shear stress
$f_{y,Lacer}$	Yield strength of lacer bar		
f_{yL}	Yield strength of locking bar		
h_k	Height of shear key		
L	Total length of joint		
L_k	Length of shear key		
n	Number of shear keys		
P	Shear load		
P_{cal}	Theoretical calculated shear capacity		
P_{FP}	First peak load		
P_{U}	Ultimate load		
s	Distance between loops		
t	Panel thickness		
$\mathbf{u}$	Displacement vector		
u_l	Longitudinal component of $\mathbf{u}$		
u_t	Transverse component of $\mathbf{u}$		
w	Crack opening		
w_l	Longitudinal crack opening		
w_t	Transverse crack opening		
W_E	Rate of external work		
W_I	Rate of internal work		
W_I^C	Rate of internal work from concrete		
W_I^s	Rate of internal work from U-bars		
W_I^{sL}	Rate of internal work from locking bar		